



Communication

A High-Performance Thin-Film Sensor in 6G for Remote Sensing of the Sea Surface

Qi Song ¹, Xiaoguang Xu ^{2,*}, Jianchen Zi ³, Jiatong Wang ⁴, Zhongze Peng ⁴, Bingyuan Zhang ¹
and Min Zhang ⁴

¹ Shandong Key Laboratory of Optical Communication Science and Technology, School of Physics Science and Information Technology, Liaocheng University, Liaocheng 252059, China; songqi@lcu.edu.cn (Q.S.); zhangbingyuan@lcu.edu.cn (B.Z.)

² Shenzhen Academy of Inspection and Quarantine, Shenzhen 518010, China

³ Jihua Laboratory, Foshan 528200, China; zijianchen@jihualab.com

⁴ State Key Laboratory of Radio Frequency Heterogeneous Integration, College of Physics and Optoelectronic Engineering, Shenzhen University, Shenzhen 518060, China; 2018172055@email.szu.edu.cn (J.W.); 2200453047@email.szu.edu.cn (Z.P.); zhangmin@szu.edu.cn (M.Z.)

* Correspondence: xu.xg@163.com

Abstract: Functional devices in the THz band will provide a highly important technical guarantee for the promotion and application of 6G technology. We sought to design a high-performance sensor with a large area, high responsiveness, and low equivalent noise power, which is stable at room temperature for long periods and still usable under high humidity; it is suitable for the environment of marine remote sensing technology and has the potential for mass production. We prepared a Te film with high stability and studied its crystallization method by comparing the sensing and detection effects of THz waves at different annealing temperatures. It is proposed that the best crystallization and detection effect is achieved by annealing at 100 °C for 60 min, with a sensitivity of up to 19.8 A/W and an equivalent noise power (NEP) of 2.8 pW Hz^{-1/2}. The effective detection area of the detector can reach the centimeter level, and this level is maintained for more than 2 months in a humid environment at 30 °C with 70–80% humidity and without encapsulation. Considering its advantages of stability, detection performance, large effective area, and easy mass preparation, our Te thin film is an ideal sensor for 6G ocean remote sensing technology.

Keywords: 6G remote sensing; THz detector; thin-film sensor; Te film; Weyl semiconductor



Citation: Song, Q.; Xu, X.; Zi, J.; Wang, J.; Peng, Z.; Zhang, B.; Zhang, M. A High-Performance Thin-Film Sensor in 6G for Remote Sensing of the Sea Surface. *Remote Sens.* **2023**, *15*, 3682. <https://doi.org/10.3390/rs15143682>

Academic Editor: Gabriel Navarro

Received: 9 June 2023

Revised: 17 July 2023

Accepted: 17 July 2023

Published: 24 July 2023



Copyright: © 2023 by the authors. Licensee MDPI, Basel, Switzerland. This article is an open access article distributed under the terms and conditions of the Creative Commons Attribution (CC BY) license (<https://creativecommons.org/licenses/by/4.0/>).

1. Introduction

Marine pollution is the result of human activities that alter the natural state of the ocean, leading to detrimental effects on marine ecosystems [1–3]. Pollution caused by harmful substances entering the marine environment can damage biological resources, endanger human health, prevent fishing and other human activities at sea, and damage the quality of seawater and the overall environment. Marine ecosystems are the most important in the world and affect the stability and security of the global ecosystem. Additionally, the survival of human beings and their economic, political, cultural, and social development are closely related to the ocean. Seawater testing is one of the most important ways to determine whether the ecology of the ocean is polluted [4,5]. “Oil in water” is the oil in the water body, which is mainly derived from industrial wastewater, domestic sewage discharge, animal decomposition, and other sources. The harm caused by oil is clear; first of all, it can consume the oxygen in the water and deteriorate its quality. Moreover, some oil becomes dispersed in the water, is partly adsorbed in suspended particles, or is in a state of emulsion in the water column, being partly dissolved in water. The oil in the water that is in the process of decomposition and oxidation by microorganisms consumes oxygen, so the deterioration in the water quality, in conjunction with oil floating on the surface of the water column,

affects the gas exchange of the air–water column interface. The formation of an oil film means that the water column cannot be quickly replenished from the CO₂ in the air, thus promoting the increased deterioration of the water quality. Second, it poisons marine life and damages fishery production. Therefore, the accurate measurement of oil composition and content in water, its detection, and the monitoring of the phenomenon of oil in water is necessary to protect the natural environment and reduce the impact of pollution on human production and life. Common methods currently used in marine oil pollutant detection mainly include the weight method, the turbidity method, chromatography, fluorescence photometry, infrared spectrophotometry, ultraviolet spectrophotometry, and other related methods of coupled technology. However, considering the use environment, detection accuracy, and detection rate, it is extremely important to research for rapid, unrestricted conditions and accurate marine water information detection technology [6–8].

Remote sensing technology is a highly effective method for maximizing the utilization of existing data and information resources. It serves as a key technology and an important tool for achieving the sustainable development of marine resources and the environment. This technology plays a crucial role in various areas such as global change, resource surveys, and environmental monitoring and prediction, which cannot be replicated by other technologies [7–9]. At the same time, the process of maintaining the sustainable development of marine resources and the environment will promote the development of information science and technology, space science and technology, environmental science and technology, and earth science [9,10]. Compared with conventional marine survey methods, marine remote sensing technology has obvious advantages, such as not being limited by geographical location, weather, and human conditions; it can cover large areas and obtain more marine information. In attempting to achieve an accurate understanding of ocean information, ocean remote sensing encounters the following challenges: the ocean reflection signal is weak and the spectral difference between phenomena is small, and ocean remote sensing requires sensors with high temporal resolutions and high spectral resolutions. The vast ocean is a body of water that is in motion all the time; for example, the sea surface wind field, wave field, current field, tides, and eddies are all simultaneously changing elements in the ocean's dynamic environment [11–14]. Therefore, the time-domain characteristics of ocean remote sensing are very important. Only by maintaining good dynamics in ocean observation can the change process of ocean elements be reflected in a timely and accurate manner. Because the spectral difference in different ocean elements is very small, only the refinement of the sensor waveband can ensure an accurate reflection of various ocean elements. In summary, it is necessary to select the appropriate waveband of electromagnetic waves to complete the remote sensing detection of marine water bodies in order to meet the spatial resolution of time and to achieve effective sensing detection capabilities and high-efficiency transmission capability [15–21].

THz technology utilizes the change in the waveform amplitude and phase of the THz pulse through the sample material to reflect the material properties of the sample. The amplitude and phase information are directly related to the absorption coefficient and refractive index of the sample so that the complex refractive index of the material can be directly obtained. This technology has a very high signal-to-noise ratio, high detection accuracy, low photon energy, and high permeability to oil contaminants such as paraffin; it has advantages that other wavelengths of light do not have, and it is, therefore, a very important means of remote sensing detection [22–24].

At the same time, sixth-generation (6G) technology adopts millimeter-wave and THz technology to optimize spatial communication transmissions, leading to transmission rates for wireless or mobile terminals of up to 11 Gb/s and meeting the requirements of remote sensing technology for fast communication. The integration of 6G remote sensing technology will enable satellite communication to cover the entire expanse between heaven and Earth. This will result in the establishment of a comprehensive network that combines ground remote sensing and ocean remote sensing, creating a global broadband network that seamlessly covers near-earth space [25]. Any location within this near-earth space

will have access to fast wireless data transmission. Due to the ubiquitous broadband network that spans heaven and Earth, the satellite remote sensing system will be able to transmit commands at any given moment, free from the constraints of geographical limitations. Similarly, the transmission of remote sensing data will not be restricted by specific time windows. With virtually limitless measurement and control resources and receiving capabilities, remote sensing technology will no longer be confined by these resources. As a result, the maximum utilization of remote sensing technology resources will be achieved.

The utilization of 6G technology in remote sensing for monitoring marine water quality has gained significant attention in the research community. The effective implementation and adoption of 6G technology heavily rely on the use of functional devices operating in the THz band. However, current THz detectors face several challenges, including limited detection area, suboptimal performance at room temperature, and difficulties in mass production. THz incoherent detectors, also known as direct detectors, can be categorized into thermal detectors and photonic detectors based on their detection principles. Thermal detectors have a relatively simple structure and can detect a wide range of the spectrum, but their sensitivity is not high. On the other hand, photonic detectors receive THz energy and convert the internal electronic state of atoms or molecules in the detector into measurable electrical signals via the photoelectric effect. These signals are then amplified to detect THz waves. Photonic detectors typically employ photoconductive and photovoltaic-type structures. Photoconductive detection, which is primarily used for single-photon detection, offers a higher response rate compared to thermal detection due to the smaller transfer rate of heat compared to electrical signals [26,27]. However, photoconductive detectors suffer from a significant drawback of a relatively high dark current, which hampers their responsiveness and detection rate. Photovoltaic-type devices partially address the issue of high dark current but are limited in their ability to achieve highly sensitive detection and are challenging to use in imaging applications. The performance of the detector largely depends on the material used, which should possess high carrier mobility, specific resistance, and unique structures. Currently, THz detectors primarily rely on IIIA-VA and IVA group semiconductor materials, semi-metallic materials, graphene, and two-dimensional materials. However, conventional semiconductors like Si or Ge with lower carrier mobility cannot achieve higher sensitivity. Semi-metallic materials, although capable of achieving broadband detection, suffer from high dark currents, limiting their sensitivity. Graphene and two-dimensional materials, despite their thinness, exhibit high resistance and increased susceptibility to defects, resulting in photodetectors based on such materials with high noise and slow response speed.

It is evident that the response rate and detection threshold of THz detectors are influenced by two crucial factors in the medium: the appropriate band gap (topology) and carrier mobility. Achieving high carrier mobility and selecting a suitable band gap are still significant challenges in enhancing detector performance. Currently, the development of THz detectors using new materials primarily concentrates on achieving micro-area responses in nanoscale sheet-like structures, while the production of large-area detectors at the millimeter scale remains limited [28–30].

A Te thin film is a chiral crystal composed of a single element, exhibiting an energy band structure typical of a conventional semiconductor. Notably, the film possesses intersections of non-interdigitated energy bands in its three-dimensional momentum space, which are protected by symmetry. These intersections give rise to Weyl points located near the band gap edge, which can be manipulated to induce various states of transport currents [31–33]. Consequently, the Te thin film serves as an ideal active layer for the fabrication of millimeter-scale detectors with effective detection areas. The performance of such detectors is heavily influenced by parameters such as the carrier mobility of the crystalline film, as well as its stability in complex environments. By annealing the Te film, we are able to crystallize it, significantly enhancing its detection capabilities. In our pursuit of advancing remote sensing technology for ocean water quality detection in the context of

6G technology, we focus on developing high-performance functional devices operating in the THz band. To this end, we have successfully prepared high-quality Te films over large areas and evaluated their detection performance in the THz band at room temperature. Additionally, we have investigated important properties such as the electromagnetic wave transmission rate and complex conductivity under different annealing conditions, thereby enhancing our understanding of the crystalline film's behavior. These findings establish crystalline films as excellent room-temperature THz detectors and demonstrate the feasibility of producing Te films in large quantities for this purpose. Our research contributes to the advancement of ocean remote sensing detection using 6G technology and furthers the development of this field.

2. Experimental Design

Figure 1 shows the experimental setup used in our study. In order to produce high-quality Te films, a two-step process was followed. Initially, Te films were deposited onto silicon substrates using magnetron sputtering. Subsequently, the devices were transferred to an annealing table shielded by nitrogen gas. These devices were then heated to various temperatures and held for different durations to complete the annealing process. Finally, the Raman spectra of the samples were analyzed under different annealing conditions to assess the quality of the annealing process.

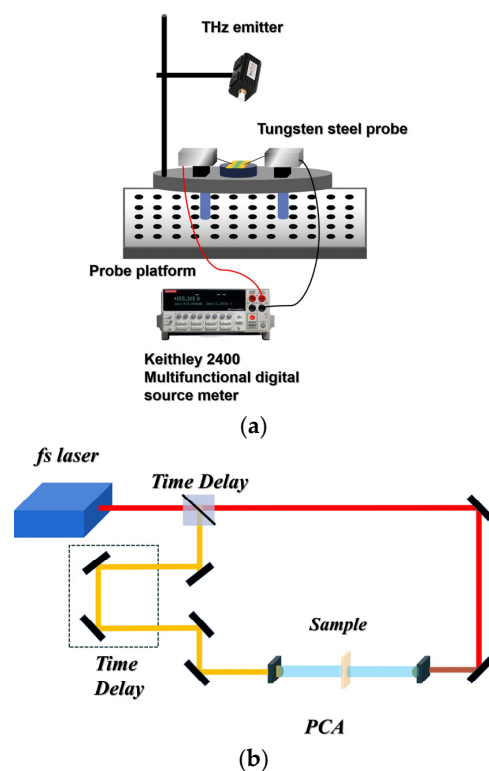


Figure 1. Experimental setup diagram. (a) Microcurrent testing probe platform; (b) THz time-domain spectrometer.

The prepared film area was $20 \text{ mm} \times 20 \text{ mm}$. The Te film was prepared using the following steps. At first, the air pressure was reduced to $1 \times 10^{-5} \text{ Pa}$, and argon was injected into the cavity. The Te target was coated using RF drive mode, and the parameters were set as follows. An argon flow rate of 30 SCCM, power of 180 W, and duration time of 1200 s were used. These coating parameters were optimized for the process.

Then, Raman spectra were measured for the different Te films. The Raman signal of a sample is commonly used to characterize the degree of crystallization and stress. In a pure lattice, the vibrational energy of the lattice is more concentrated, resulting in a

narrow spectral peak width. Conversely, if the lattice is damaged or poorly crystallized, the vibrational energy after excitation spreads over a wider range, leading to a broadened spectral peak width. When the lattice is subjected to compression or stretching without being destroyed, stress is generated, which is manifested as a peak displacement. Therefore, the intensity and width of the Raman peak are typically used to determine the degree of crystallization of the fabricated film. A higher peak intensity and narrower peak width correspond to stronger crystallization of the sample. It can be concluded that the Te films exhibit optimal crystallinity when annealed at a temperature of 100 °C for 30 min. The degree of crystallization decreases when the energy provided to Te is insufficient or excessive, either without annealing or when the annealing temperature exceeds 100 °C.

Furthermore, the polarization Raman results were also measured at different annealing temperatures. The laser incident on the sample with varying polarization directions exhibited distinct polarization characteristics. The formation of a polarization sheet-like effect by the main atomic chain was more pronounced in films with higher crystallization degrees, indicating a higher polarization degree of polarization Raman. The highest polarization was observed at an annealing temperature of 100 °C, as determined by analyzing the peak results [34,35].

In addition, the analog degree of polarization (*DOP*) was defined to calculate the polarization sensitivity of the device [36]:

$$DOP = \frac{|M_{\max} - M_{\min}|}{|M_{\max} + M_{\min}|} \quad (1)$$

where M_{\max} and M_{\min} are the maximum and minimum Raman intensities, which are parallel and perpendicular to the polarization direction of the laser, respectively. According to Equation (5), the maximum *DOP* of the device was 0.19, 0.16, and 0.13. It can be seen that the degree of crystallization of the sample annealed at 100 °C was better than that of the non-annealed sample and the sample annealed at 200 °C. The polarization Raman experiments provided clear evidence of the enhanced crystallization of Te films annealed at 100 °C.

The Raman spectroscopy results and scanning electron microscopy (SEM) images of the Te thin films are presented in Figure 2. The film thickness was determined using the SEM analysis of the cut surface. The Si substrate, which was coated with the thin film, was cut from the back side and positioned upright to measure the film thickness in the cross-section. The figure demonstrates that the coating thickness was consistent and measured at 4.24 μm.

Finally, copper (Cu) electrodes were fabricated on the prepared Te films with an electrode pitch of 5 mm. The fabrication process involved the following steps. First, the air pressure was reduced to 1×10^{-5} Pa, and argon gas was introduced into the cavity. The Cu target was then coated using a direct current (DC) drive mode. The specific parameters for this process were set as follows: an argon flow rate of 15 SCCM, a current of 0.2 A, and a duration time of 90 s.

In order to investigate the properties of films in the THz band under various crystallization conditions, such as transmittance and complex conductivity, the transmittance spectra of the films were examined using THz-TDS. The laser used in THz-TDS had a central wavelength of 780 nm, a repetition frequency of 80 MHz, a pulse width of 90 fs, and a spectral width of 7 nm. Figure 3 illustrates the characterization of Te thin films in the THz band. The results of the tests indicated that the lowest THz transmittance was observed at an annealing temperature of 100 °C. This finding suggests that the degree of crystallization was optimal at this temperature, as the atoms became regularly arranged and the carriers were more uniformly bound around them. Consequently, the transmission rate of the incident THz wave decreased. The experimental data revealed the transmission rates of Te films with thicknesses of 4.24 μm and varying degrees of crystallinity (annealed at 100 °C, 200 °C, and no annealing) in the THz range from 56% to 78%, 61% to 85%, and 67% to 94%, respectively.

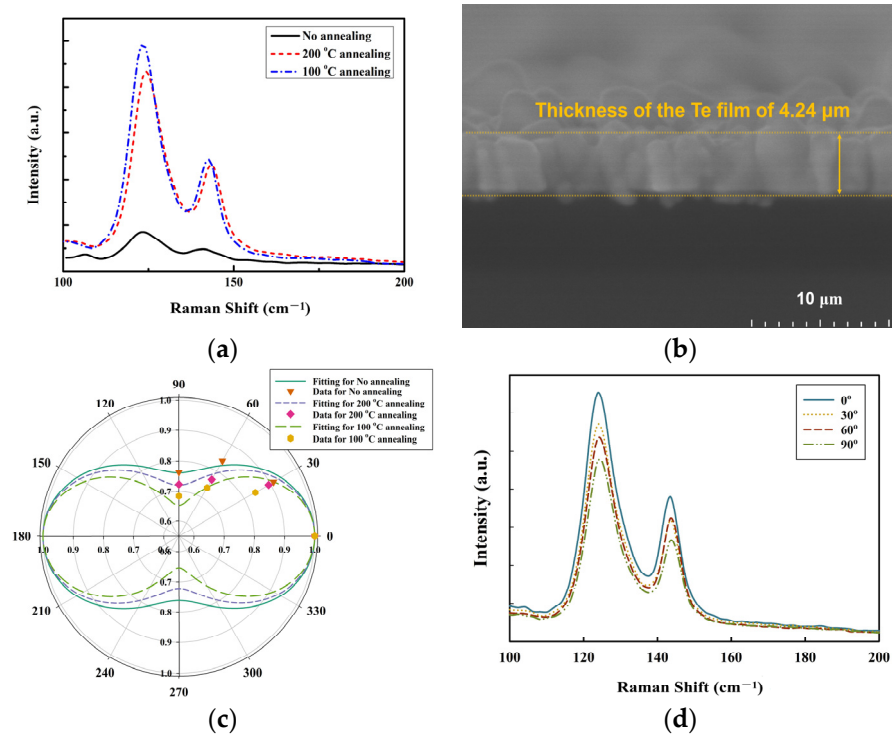


Figure 2. Characterization of Te thin films. (a) Raman spectra of Te films at different annealing temperatures. (b) SEM images of film thickness. (c) Raman spectral intensity and incident angle of samples with different annealing temperatures and polarization. (d) Raman spectra of different laser polarization incidence for 100 °C annealing temperature Te film.

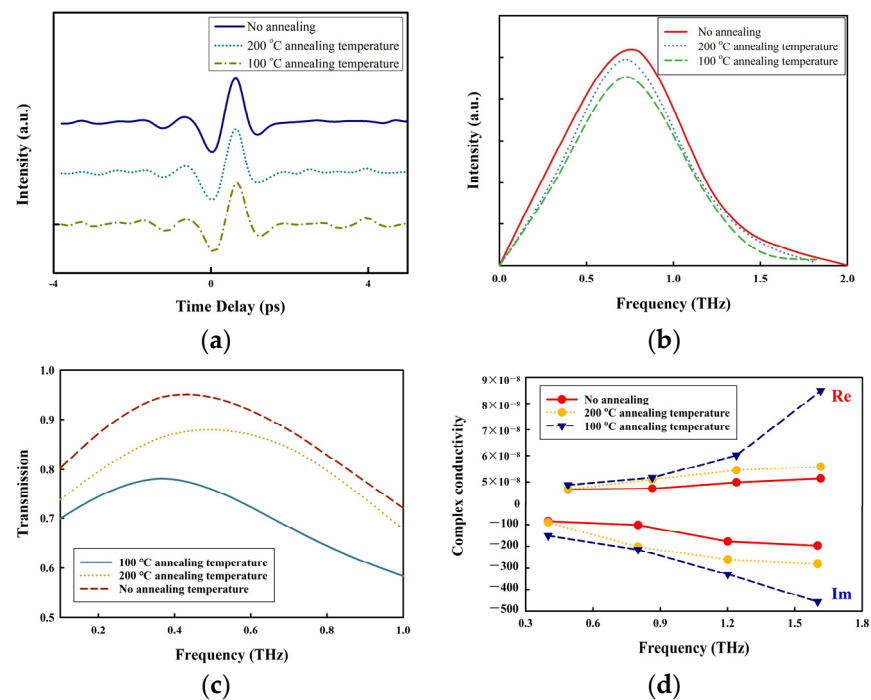


Figure 3. Characterization of Te thin films in the THz band. (a) THz pulses through thin films at different annealing temperatures. (b) Fourier transform results of (a,c) THz transmittance of thin films with different annealing temperatures. (d) Complex conductivity of thin films with different annealing temperatures in the THz band.

Furthermore, variations in the degree of crystallinity result in distinct atomic binding capabilities of the carriers, consequently leading to notable disparities in the complex conductivity of the films. It is observed that a higher degree of crystallization corresponds to a greater magnitude of complex conductivity. Figure 2b shows the complex conductivity of the Te nanofilm at room temperature. The ordinary Drude equation was also employed to fit the frequency dependence of conductivity [37]:

$$\sigma(\omega) = \sigma_0 \frac{1}{1 - i\omega\tau} \quad (2)$$

Here, ω indicates the frequency of the THz wave, τ is the quasi-particle relaxation time, and σ_0 is the DC conductivity. The results of the complex conductivity in the THz band show the best complex conductivity parameters at the preferred annealing temperature, i.e., 60 min at 100 °C. The Te films produced under these specific conditions exhibit enhanced suitability for devices operating within the THz frequency range.

3. Results and Discussion

The main parameters of THz detectors are total noise (V_n), photoresponsivity (R_A), noise equivalent power (NEP), detection rate (D^*), and response time.

Detector total noise (V_n) is inherent to the detector, and it is impossible to eliminate it artificially. Noise includes external noise (man-made noise and natural noise) and internal noise (scattered particle noise, thermal noise, etc.). The device that generates an alteration in the current or voltage as a result of light reception is referred to as a signal detector. Noise, on the other hand, is an irregular fluctuation in the output that occurs alongside the signal. Typically, noise is regarded as random, and its average over time is zero. Consequently, the magnitude of noise cannot be determined via time averaging. As the total power of noise is the sum of different noise powers, the root mean square noise voltage serves as a suitable measure for assessing the magnitude of noise [38]. V_n mainly includes the thermal Johnson–Nyquist noise (V_t) and the dark current noise (V_b) introduced by the addition of the bias voltage, which is defined as follows [38]:

$$v_n = \left(v_t^2 + v_b^2 \right)^{1/2} = \left(4k_B T r + 2q I_d r^2 \right)^{1/2} \quad (3)$$

where k_B is the Boltzmann constant, T is the absolute detector temperature in Kelvin, r represents the resistance of the device in Ω , q is the fundamental charge, and I_d is the dark current of the device. The thermal Johnson–Nyquist noise is caused by the random thermal motion of carriers inside the material due to thermal stirring, independent of the added voltage, and the total noise V_n rises with an increase in voltage bias, which is caused by an increase in v_b due to the change in voltage bias.

Photoresponsivity (R_A) is the changing current of the device under illumination, defined as the photocurrent generated per unit of optical power, which can be expressed as follows [38]:

$$R_A = \frac{I}{P} \quad (4)$$

where P is the power of the THz source. Thus, the equation represents the effective detection response of the detector to THz waves, and the higher optical responsiveness of the device shows its higher photoelectric conversion efficiency.

The noise equivalent power (NEP) is a metric that quantifies the sensitivity of a detector by measuring the minimum optical power it can detect. It is calculated by dividing the signal optical power by the square root of the bandwidth and the signal-to-noise ratio. A lower NEP indicates a higher ability to detect weak signals [38]:

$$NEP = \frac{v_n}{R} \quad (5)$$

The detection rate (D^*) is a crucial parameter that measures the normalized signal-to-noise performance of a detector. It is directly linked to the equivalent noise power, meaning that a higher detection rate indicates a better detection performance of the device. D^* serves as a parameter for evaluating the sensitivity of various detectors with different effective areas, allowing for a standardized assessment of their detection capabilities., defined as follows [38]:

$$D^* = \sqrt{S}/NEP \quad (6)$$

where S is the detection effective area and the normalized detection rate D^* is often used to compare the detection performance of the different detectors.

The speed at which a detector responds is a crucial factor for its performance. This is particularly important for applications such as photoelectric detection, remote sensing, and fast imaging. The response time refers to the time it takes for the detector to generate a specific output in response to radiation. This response time is determined by the rise and fall times of the detector's output signal when a step signal light is inputted. In general, the rise time is the time it takes for the detector output pulse signal to increase from 10% to 90% of the leading edge, whereas the fall time is the time it takes for the signal to decrease from 90% to 10% of the trailing edge.

The experimental setup is schematically shown in Figure 1a. First, all test benches were strictly grounded to prevent electrostatic generation, and the THz detector was placed in the center of the probe platform with two tungsten probes (with a 1 μm tip) in contact with the metal electrodes of the device and connected to a digital source meter. The digital source meter (Keithley2400) applied a voltage range of 0–200 V and had a current test accuracy of 2 nA. A TeraSense IMPATT diode at 0.1 THz with an output power of 70 mW was employed as the THz emitter. The THz beam was not focused on the sample. A copper conical horn antenna was used for the coupling output. In addition, a THz power meter (ELVA-1 DPM R-1612) was first used to measure the THz power before starting the experiment, when the distance between the emitting end of the IMPATT diode and the power meter was equal to the distance where the sample was to be placed on the probe platform. The THz response of the device was obtained from the tested I-V curve.

The response characteristics of three large-area Te films with different degrees of crystallization to THz waves were tested in the experiment. The noise characteristics are shown in Figure 4. For the Te films annealed at 100 $^{\circ}\text{C}$, 200 $^{\circ}\text{C}$, and no annealing, the total noise (V_n) was $1 \times 10^{-7} \text{ V}/\text{Hz}^{1/2}$, $1.12 \times 10^{-7} \text{ V}/\text{Hz}^{1/2}$, $1.32 \times 10^{-7} \text{ V}/\text{Hz}^{1/2}$, respectively. The experimental results show that a higher degree of Te crystallization leads to lower noise. The increase in V_n with increasing bias is mainly caused by an increase in V_b .

In addition, Figure 4 shows the R_A , NEP , and D^* of the device at different bias voltages when operating in the 6G experimental band, i.e., 0.1 THz, at room temperature (26 $^{\circ}\text{C}$, 70% air humidity). For 100 $^{\circ}\text{C}$ annealing temperature, 200 $^{\circ}\text{C}$ annealing temperature, and no annealing temperature, the R_A of the Te films at a bias voltage of 20 V were 19.8 A/W, 18.2 A/W, and 13.5 A/W. The NEP are $2.8 \text{ pW}\cdot\text{Hz}^{-1/2}$, $3.1 \text{ pW}\cdot\text{Hz}^{-1/2}$, and $3.6 \text{ pW}\cdot\text{Hz}^{-1/2}$. The final detection rates D^* were $1.85 \times 10^{10} \text{ cm Hz}^{-1/2} \text{ W}^{-1}$, $1.79 \times 10^{10} \text{ cm Hz}^{-1/2} \text{ W}^{-1}$, and $1.53 \times 10^{10} \text{ cm Hz}^{-1/2} \text{ W}^{-1}$, respectively.

We tested the THz detection performance of Te films under different annealing conditions and found that the better the crystallization effect of the Te films, the higher the detection performance, which was reflected in the parameters, namely, the large photoresponsivity R_A , small NEP , large D^* , and small overall noise. Thin films with a higher degree of crystallization exhibited higher carrier migration efficiency and a more beneficial energy band structure of the Weyl semiconductor for THz detection, i.e., the unique optical selection rules followed by Te during the leap within a single Weyl cone and between different Weyl cones. The crystalline Weyl semiconductor Te exhibited ultra-high mobility, a strain- and thickness-tunable band gap, and a two-dimensional layered structure with outstanding air stability. These results eventually led to a high light-current response from Te. So, the detection efficiency of the crystallized Te film was further enhanced, and consid-

ering its excellent stability and non-hygroscopic properties, it can be used in high-humidity environments, making it an ideal detector for ocean remote sensing.

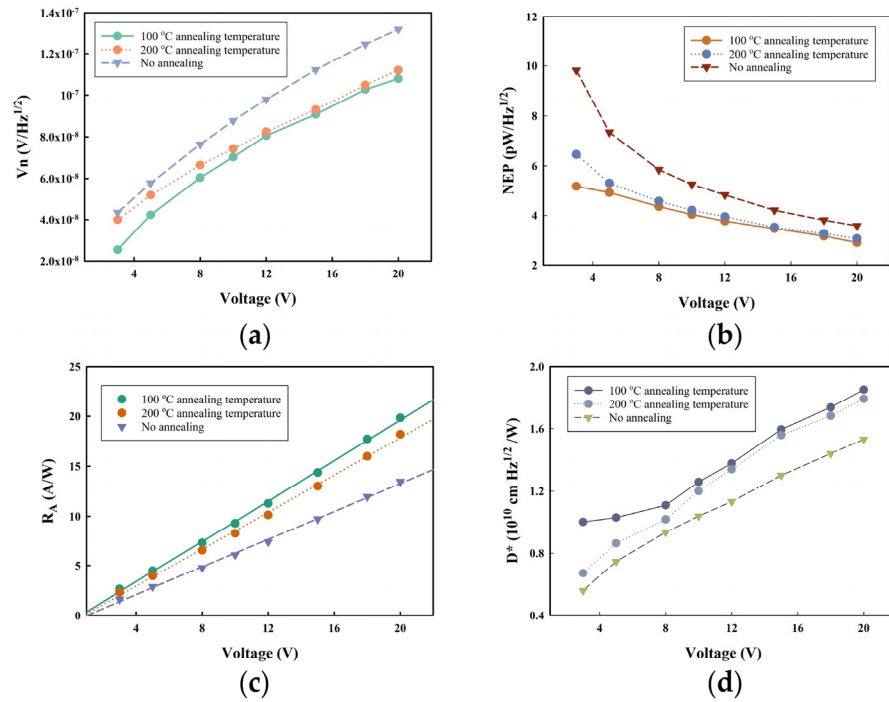


Figure 4. Detection performance for the 100 °C annealing temperature, 200 °C annealing temperature, and no annealing temperature Te films at 0.1 THz. (a) Detector total noise (V_n); (b) photoresponsivity (R_A); (c) noise equivalent power (NEP); (d) detectivity (D^*). Typical calculated (lines) and measured (dots).

The response rates of devices with Te thin films annealed at 100 °C, 200 °C, and no annealing of 78 ms, 93 ms, and 104 ms were obtained due to the limitation of the test sampling rate (as shown in Figure 5). The results of the response rate correspond to the detection performance and Raman test results. In addition, the test can be more accurate if it is performed at a high current sampling time.

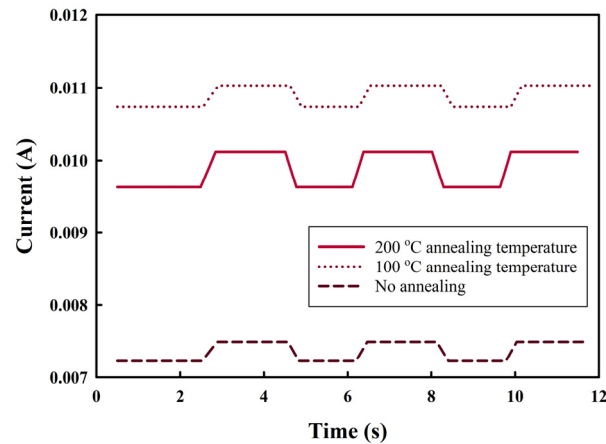


Figure 5. Response times of different Te films.

The stability of the samples was tested. After two months of exposure to complete air in an environment with a humidity of 70–80% and a temperature of 30 °C, there was no significant change in the light and dark currents of the device. Therefore, crystalline Te

films are well suited for use in real humid environments and are very suitable for use as detectors for ocean remote sensing.

In addition, we compared the main performances of THz detectors in recent years, as shown in Table 1. Due to the limited application of ocean remote sensing technology, it must be employed in humid environments with water vapor and a large effective detection area, at least at the millimeter level. Furthermore, its photoresponsivity and NEP have certain advantages. Considering the criteria of mass production, room temperature stability, and use in humid environments, our Te thin-film detector is more appropriate for environments in which marine remote sensing technology is used. Therefore, the simple crystalline Te thin film is an ideal sensor for 6G ocean remote sensing technology.

Table 1. The main performance of THz detectors in recent years.

Materials	Detection Frequency	Photoresponsivity	NEP (pW/Hz ^{1/2})	Effective Detection Area	Ref
Bi ₂ Se ₃	0.3 THz	0.29×10^{-2} V/W	0.36	Nanoscale	[39]
PtTe ₂	0.12 THz	1400 V/W	10	Nanoscale	[40]
PdTe ₂	0.3 THz	1.3×10^{-8} V/W	57	Nanoscale	[41]
PbS	0.14 THz	3.12 A/W	0.661	Millimeter scale	[42]
WTe ₂	0.1 THz	8.78 A/W	0.74	Millimetre scale	[43]
MoTe ₂	0.1 THz	4 A/W	9.74	Millimetre scale	[44]
Te crystal	0.305 THz	9.83 A/W	0.6	Nanoscale	[45]
Bi ₈₈ Sb ₁₂	0.14 THz	12–20 mV/W	770	Micron scale	[46]
NbIrTe ₄	0.03 THz	5.7×10^4 V/W	-	Nanoscale	[47]
EuSn ₂ As ₂	0.02 THz	0.2 A/W	30	Nanoscale	[48]
NbSe ₂	0.173 THz	7.8×10^6 V/W	0.05	Nanoscale	[49]
MAPbI ₃	0.1 THz	88.8 μ A/W	2160	Nanoscale	[50]
VSe ₂	0.256 THz	1.3×10^3 A/W	0.02	Nanoscale	[51]
GaN	0.21~0.23 THz	4.9 kV/W	72	Nanoscale	[52]
GO/Bi	0.22 THz	0.226 V/W	1340	Nanoscale	[53]
multigate graphene	0.3 THz	1.9 mA/W	670	Nanoscale	[54]
Black Phosphorus	0.12 THz	297 V/W	58	Nanoscale	[55]
antiferromagnetic/heavy metal	0.45 THz	2500 V/W	-	Nanoscale	[56]
bilayer graphene	0.13THz	>4 kV/W	0.2	Microscale	[57]
Si-metal	0.1–1.5 THz	40 mA/W	42	Millimeter scale	[58]
Te	0.1 THz	19.8 A/W	2.8	Centimeter scale	This Work

4. Conclusions

The utilization of remote sensing technology to assess marine water quality for 6G technology has gained significant attention in academic research. However, a notable gap exists in the availability of high-performance sensors that possess a large area at the centimeter level, exhibit high responsiveness, low NEP, high stability, and have the potential for mass production in a humid environment. In order to address this issue, we developed a marine remote sensing sensor specifically designed for 6G technology. This sensor incorporates a highly stable Te film, and we conducted a comprehensive study on its crystallization method, with a particular focus on comparing the sensing detection of THz waves under varying annealing temperatures. Our findings revealed the optimal crystallization method for this sensor, thereby contributing to the advancement of remote sensing technology for marine water quality assessment in the context of 6G technology. The best crystallization and detection effect was obtained at 100 °C annealing for 60 min, the R_A was up to 19.8 A/W, the NEP was 2.8 pW Hz^{-1/2}, the effective detection area of the detector could reach the centimeter level, and it was maintained for more than 2 months without encapsulation in a humid environment at 30 °C and 70–80% humidity. Furthermore, the response time of the film was measured as 78 ms. Taking into account its notable benefits, such as stability, detection performance, rapid response time, expansive

effective area, and straightforward mass production, the crystalline Te large-area film has emerged as a sensor for the advancement of 6G ocean remote sensing technology.

Author Contributions: Q.S.: formal analysis, investigation, data curation, methodology, writing—original draft. X.X.: writing—review and editing, funding acquisition. J.Z.: project administration. Z.P. and J.W.: formal analysis, investigation, methodology. B.Z. and M.Z.: resources, formal analysis, supervision, methodology. All authors have read and agreed to the published version of the manuscript.

Funding: This research was funded by the National Natural Science Foundation of China, grant number 12104314, the Key Laboratory of Optoelectronic Devices and Systems of Ministry of Education and Guangdong Province, Research Foundation of Liaocheng University (No. 318052316) and Guangdong Basic and Applied Basic Research Foundation, grant number 2020A1515110709.

Data Availability Statement: The data that support the findings of this study are available from the corresponding author upon reasonable request.

Acknowledgments: The authors acknowledge the assistance from the Photonics Center of Shenzhen University.

Conflicts of Interest: The authors declare no conflict of interest.

References

1. Belkin, I.M. Remote Sensing of Ocean Fronts in Marine Ecology and Fisheries. *Remote Sens.* **2021**, *13*, 883. [[CrossRef](#)]
2. Grotte, M.E.; Birkeland, R.; Honore-Livermore, E.; Bakken, S.; Garrett, J.L.; Prentice, E.F.; Sigernes, F.; Orlandic, M.; Gravidahl, J.T.; Johansen, T.A. Ocean Color Hyperspectral Remote Sensing With High Resolution and Low Latency—The HYPSON-1 CubeSat Mission. *IEEE Trans. Geosci. Remote Sens.* **2021**, *60*, 1–19. [[CrossRef](#)]
3. Kramer, S.J.; Siegel, D.A.; Maritorena, S.; Catlett, D. Modeling surface ocean phytoplankton pigments from hyperspectral remote sensing reflectance on global scales. *Remote Sens. Environ.* **2022**, *270*, 112879. [[CrossRef](#)]
4. Su, H.; Qin, T.; Wang, A.; Lu, W. Reconstructing Ocean Heat Content for Revisiting Global Ocean Warming from Remote Sensing Perspectives. *Remote Sens.* **2021**, *13*, 3799. [[CrossRef](#)]
5. Liu, H.; He, X.; Li, Q.; Kratzer, S.; Wang, J.; Shi, T.; Hu, Z.; Yang, C.; Hu, S.; Zhou, Q.; et al. Estimating ultraviolet reflectance from visible bands in ocean colour remote sensing. *Remote Sens. Environ.* **2021**, *258*, 112404. [[CrossRef](#)]
6. Seydi, S.T.; Hasanlou, M.; Amani, M.; Huang, W. Oil Spill Detection Based on Multiscale Multidimensional Residual CNN for Optical Remote Sensing Imagery. *IEEE J. Sel. Top. Appl. Earth Obs. Remote Sens.* **2021**, *14*, 10941–10952. [[CrossRef](#)]
7. Wang, T.; Yu, P.; Wu, Z.; Lu, W.; Liu, X.; Li, Q.P.; Huang, B. Revisiting the Intraseasonal Variability of Chlorophyll-a in the Adjacent Luzon Strait With a New Gap-Filled Remote Sensing Data Set. *IEEE Trans. Geosci. Remote Sens.* **2021**, *60*, 1–11. [[CrossRef](#)]
8. Hsu, T.Y.; Chang, Y.; Lee, M.A.; Wu, R.F.; Hsiao, S.C. Predicting skipjack tuna fishing grounds in the Western and Central Pacific Ocean based on high-spatial-temporal-resolution satellite data. *Remote Sens.* **2021**, *13*, 861. [[CrossRef](#)]
9. Fan, Y.; Li, W.; Chen, N.; Ahn, J.-H.; Park, Y.-J.; Kratzer, S.; Schroeder, T.; Ishizaka, J.; Chang, R.; Stamnes, K. OC-SMART: A machine learning based data analysis platform for satellite ocean color sensors. *Remote Sens. Environ.* **2021**, *253*, 112236. [[CrossRef](#)]
10. Xie, T.; Ouyang, R.; Perrie, W.; Zhao, L.; Zhang, X. Proof and Application of Discriminating Ocean Oil Spills and Seawater Based on Polarization Ratio Using Quad-Polarization Synthetic Aperture Radar. *Remote Sens.* **2023**, *15*, 1855. [[CrossRef](#)]
11. Silva, G.S.M.; Garcia, C.A.E. Evaluation of ocean chlorophyll-a remote sensing algorithms using in situ fluorescence data in Southern Brazilian Coastal Waters. *Ocean. Coast. Res.* **2021**, *69*. [[CrossRef](#)]
12. Seela, B.K.; Janapati, J.; Unnikrishnan, C.K.; Lin, P.-L.; Le Loh, J.; Chang, W.-Y.; Kumar, U.; Reddy, K.K.; Lee, D.-I.; Reddy, M.V. Raindrop Size Distributions of North Indian Ocean Tropical Cyclones Observed at the Coastal and Inland Stations in South India. *Remote Sens.* **2021**, *13*, 3178. [[CrossRef](#)]
13. Ma, Y.; Yin, W.; Guo, Z.; Xuan, J. The Ocean Surface Current in the East China Sea Computed by the Geostationary Ocean Color Imager Satellite. *Remote Sens.* **2023**, *15*, 2210. [[CrossRef](#)]
14. Kuroda, H.; Setou, T. Extensive Marine Heatwaves at the Sea Surface in the Northwestern Pacific Ocean in Summer 2021. *Remote Sens.* **2021**, *13*, 3989. [[CrossRef](#)]
15. Liu, H.; Li, X.; Cheng, Z.; Liu, T.; Zhai, J.; Hu, H. Polarization Maintaining 3-D Convolutional Neural Network for Color Polarimetric Images Denoising. *IEEE Trans. Instrum. Meas.* **2023**, *72*, 1–9. [[CrossRef](#)]
16. Li, X.; Hu, H.; Zhao, L.; Wang, H.; Yu, Y.; Wu, L.; Liu, T. Polarimetric image recovery method combining histogram stretching for underwater imaging. *Sci. Rep.* **2018**, *8*, 12430. [[CrossRef](#)]
17. Wang, H.; Li, J.; Hu, H.; Jiang, J.; Li, X.; Zhao, K.; Cheng, Z.; Sang, M.; Liu, T. Underwater Imaging by Suppressing the Backscattered Light Based on Mueller Matrix. *IEEE Photonics J.* **2021**, *13*, 7800106. [[CrossRef](#)]
18. Li, X.; Zhang, L.; Qi, P.; Zhu, Z.; Xu, J.; Liu, T.; Zhai, J.; Hu, H. Are Indices of Polarimetric Purity Excellent Metrics for Object Identification in Scattering Media? *Remote Sens.* **2022**, *14*, 4148. [[CrossRef](#)]

19. Li, X.; Hu, H.; Zhao, L.; Wang, H.; Han, Q.; Cheng, Z.; Liu, T. Pseudo-polarimetric Method for Dense Haze Removal. *IEEE Photonics J.* **2019**, *11*, 6900611. [[CrossRef](#)]
20. Li, X.; Hu, H.; Wu, L.; Liu, T. Optimization of instrument matrix for Mueller matrix ellipsometry based on partial elements analysis of the Mueller matrix. *Opt. Express* **2017**, *25*, 18872–18884. [[CrossRef](#)]
21. Li, X.; Han, Y.; Wang, H.; Liu, T.; Chen, S.-C.; Hu, H. Polarimetric Imaging Through Scattering Media: A Review. *Front. Phys.* **2022**, *10*, 815296. [[CrossRef](#)]
22. Liao, S.; Wu, J.; Li, J.; Konstantin, K. Information-Centric Massive IoT-Based Ubiquitous Connected VR/AR in 6G: A Proposed Caching Consensus Approach. *IEEE Internet Things* **2021**, *8*, 5172–5184. [[CrossRef](#)]
23. Rajesh, G.; Dakshita, R.; Sudeep, T. 6G-enabled Edge Intelligence for Ultra-Reliable Low Latency Applications: Vision and Mission. *Comput. Stand Inter.* **2021**, *77*, 103521.
24. Qi, W.; Li, Q.; Song, Q.; Guo, L.; Jamalipour, A. Extensive Edge Intelligence for Future Vehicular Networks in 6G. *IEEE Wirel Commun.* **2021**, *28*, 128–135. [[CrossRef](#)]
25. Guo, H.; Zhou, X.; Liu, J.; Zhang, Y. Vehicular intelligence in 6G: Networking communications and computing. *Veh. Commun.* **2022**, *33*, 100399. [[CrossRef](#)]
26. Shilpa, T.; Nageen, H.; Hosein, N.; Feng, X.; Geng, W.; Vida, I. 6G: Connectivity in the Era of Distributed Intelligence. *IEEE Commun. Mag.* **2021**, *59*, 45–50.
27. Huang, X.; Zhang, K.; Wu, F.; Leng, S. Collaborative Machine Learning for Energy-Efficient Edge Networks in 6G. *IEEE Netw.* **2021**, *35*, 12–19. [[CrossRef](#)]
28. Liu, D.F.; Liang, A.J.; Liu, E.K.; Xu, Q.N.; Li, Y.W.; Chen, C.; Pei, D.; Shi, W.J.; Mo, S.K.; Dudin, P.; et al. Magnetic Weyl semimetal phase in a Kagome crystal. *Science* **2019**, *365*, 1282–1285. [[CrossRef](#)]
29. Rees, D.; Manna, K.; Lu, B.; Morimoto, T.; Borrmann, H.; Felser, C.; Moore, J.E.; Darius, T.; Orenstein, J. Helicity-dependent photocurrents in the chiral Weyl semimetal RhSi. *Sci. Adv.* **2020**, *6*, eaba0509. [[CrossRef](#)]
30. Morali, N.; Batabyal, R.; Nag Pranab, K.; Liu, E.; Xu, Q.; Sun, Y.; Yan, B.; Felser, C.; Avraham, N.; Beidenkopf, H. Fermi-arc diversity on surface terminations of the magnetic Weyl semimetal Co₃Sn₂S₂. *Science* **2019**, *365*, 1286–1291. [[CrossRef](#)]
31. Chen, J.; Zhang, T.; Wang, J.; Xu, L.; Lin, Z.; Liu, J.; Wang, C.; Lau, S.P.; Zhang, W.; Chhowalla, M.; et al. Topological phase change transistors based on tellurium Weyl semiconductor. *Sci. Adv.* **2022**, *8*, eabn3837. [[CrossRef](#)]
32. Zhang, X.; Yang, Y.; Li, Z.; Liu, X.; Zhang, C.; Peng, S.; Han, J.; Zhou, H.; Gou, J.; Xiu, F.; et al. Weyl Semiconductor Te/Sb₂Se₃ Heterostructure for Broadband Photodetection and Its Binary Photoresponse by C₆₀ as Charge-Regulation Medium. *Adv. Opt. Mater.* **2021**, *9*, 2101256. [[CrossRef](#)]
33. Zhang, N.; Zhao, G.; Li, L.; Wang, P.; Xie, L.; Cheng, B.; Li, H.; Lin, Z.; Xi, C.; Ke, J.; et al. Magnetotransport signatures of Weyl physics and discrete scale invariance in the elemental semiconductor tellurium. *Proc. Natl. Acad. Sci. USA* **2020**, *117*, 11337–11343. [[CrossRef](#)]
34. Liu, N.; Wang, Y.; Li, W.B.; Zhang, L.Y.; He, S.K.; Zhao, J.K.; Zhao, J.J. Thermal stability study of Weyl semimetal WTe₂/Ti heterostructures by Raman scattering. *Acta Phys. Sin. Ch. Ed.* **2022**, *71*, 197501. [[CrossRef](#)]
35. Lu, W.; Zhang, Y.D.; Zhu, Z.S.; Lai, J.W.; Zhao, C.; Liu, X.F.; Liu, J.; Sun, D. Thin tungsten telluride layer preparation by thermal annealing. *Nanotechnology* **2017**, *27*, 414006. [[CrossRef](#)] [[PubMed](#)]
36. Song, Q.; Chai, L.; Liu, W.; Ma, Q.; Li, Y.; Hu, M. THz polarization-sensitive characterization of a large-area multilayer rhenium diselenide nanofilm. *Nanotechnology* **2019**, *30*, 505203. [[CrossRef](#)] [[PubMed](#)]
37. Song, Q.; Chen, H.; Zhang, M.; Li, L.; Yang, J.; Yan, P. Broadband electrically controlled bismuth nanofilm THz modulator. *APL Photonics* **2021**, *6*, 056103. [[CrossRef](#)]
38. Tong, J.; Suo, F.; Zhang, T.; Huang, Z.; Chu, J.; Zhang, D.H. Plasmonic semiconductor nanogroove array enhanced broad spectral band millimetre and terahertz wave detection. *Light Sci. Appl.* **2021**, *10*, 58. [[CrossRef](#)] [[PubMed](#)]
39. Tang, W.W.; Politano, A.; Guo, C.; Guo, W.L.; Liu, C.L.; Wang, L.; Chen, X.S.; Lu, W. Ultrasensitive Room-Temperature Terahertz Direct Detection Based on a Bismuth Selenide Topological Insulator. *Adv. Funct. Mater.* **2018**, *28*, 1801786. [[CrossRef](#)]
40. Xu, H.; Guo, C.; Zhang, J.; Guo, W.; Kuo, C.-N.; Lue, C.S.; Hu, W.; Wang, L.; Chen, G.; Politano, A.; et al. PtTe₂-Based Type-II Dirac Semimetal and Its van der Waals Heterostructure for Sensitive Room Temperature Terahertz Photodetection. *Small* **2019**, *15*, 1903362. [[CrossRef](#)]
41. Guo, C.; Hu, Y.; Chen, G.; Wei, D.; Zhang, L.; Chen, Z.; Guo, W.; Xu, H.; Kuo, C.-N.; Lue, C.S.; et al. Anisotropic ultrasensitive PdTe₂-based phototransistor for room-temperature long-wavelength detection. *Sci. Adv.* **2020**, *6*, eabb6500. [[CrossRef](#)]
42. Song, Q.; Xu, Y.F.; Zhou, Z.W.; Liang, H.W.; Zhang, M.Y.; Zhu, G.Y.; Yang, J.B.; Yan, P.G. Terahertz Detectors for 6G Technology Using Quantum Dot 3D Concave Convergence Microwheel Arrays. *ACS Photonics* **2022**, *9*, 2520–2527. [[CrossRef](#)]
43. Song, Q.; Zhou, Z.; Zhu, G.; Liang, H.; Zhang, M.; Zhang, B.; Liu, F.; Yan, P. Microdisk array based Weyl semimetal nanofilm terahertz detector. *Nanophotonics* **2022**, *11*, 3595–3602. [[CrossRef](#)]
44. Zhou, Z.; Song, Q.; Xu, Y.; Liang, H.; Zhang, M.; Zhang, B.; Yan, P. Magnetron sputtering deposited large-scale Weyl semimetal THz detector. *Infrared Phys. Technol.* **2022**, *121*, 104060. [[CrossRef](#)]
45. Ma, W.N.; Gao, Y.Q.; Shang, L.Y.; Zhou, W.; Yao, N.J.; Jiang, L.; Qiu, Q.X.; Li, J.B.; Shi, Y.; Hu, Z.G.; et al. Ultrabroadband Tellurium Photoelectric Detector from Visible to Millimeter Wave. *Adv. Sci.* **2021**, *9*, 2103873. [[CrossRef](#)]

46. Khodzitsky, M.; Tukmakova, A.; Zykov, D.; Novoselov, M.; Tkhorzhevskiy, I.; Sedinin, A.; Novotelnova, A.; Zaitsev, A.; Demchenko, P.; Makarova, E.; et al. THz room-temperature detector based on thermoelectric frequency-selective surface fabricated from Bi₈₈Sb₁₂ thin film. *Appl. Phys. Lett.* **2021**, *119*, 164101. [[CrossRef](#)]
47. Zhang, J.; Zhang, T.; Yan, L.; Zhu, C.; Shen, W.; Hu, C.; Lei, H.; Luo, H.; Zhang, D.; Liu, F.; et al. Colossal Room-Temperature Terahertz Topological Response in Type-II Weyl Semimetal NbIrTe₄. *Adv. Mater.* **2022**, *34*, 2204621. [[CrossRef](#)]
48. Liu, C.; Liu, Y.; Chen, Z.; Zhang, S.; Shi, C.; Li, G.; Yu, X.; Xu, Z.; Zhang, L.; Zhao, W.; et al. A candidate material EuSn₂As₂-based terahertz direct detection and imaging. *npj 2D Mater. Appl.* **2022**, *6*, 26. [[CrossRef](#)]
49. Li, J.; Ma, W.; Jiang, L.; Yao, N.; Deng, J.; Qiu, Q.; Shi, Y.; Zhou, W.; Huang, Z. High Performance of Room-Temperature NbSe₂ Terahertz Photoelectric Detector. *ACS Appl. Mater. Interfaces* **2022**, *14*, 14331–14341. [[CrossRef](#)]
50. Li, J.; Zou, Y.; Hu, D.; Gu, Y.; Han, Z.; Liu, J.; Xu, X. Enhanced room-temperature terahertz detection and imaging derived from anti-reflection 2D perovskite layer on MAPbI₃ single crystals. *Nanoscale* **2022**, *14*, 6109–6117. [[CrossRef](#)]
51. Li, J.; Jiang, L.; Ma, W.; Wu, T.; Qiu, Q.; Shi, Y.; Zhou, W.; Yao, N.; Huang, Z. VSe₂ Nanosheets for Broadband Photodetection from Visible to Terahertz. *ACS Appl. Nano Mater.* **2022**, *5*, 5158–5167. [[CrossRef](#)]
52. Huang, Z.; Yan, W.; Li, Z.; Dong, H.; Yang, F.; Wang, X. High-Responsivity, Low-Leakage Current, Ultra-Fast Terahertz Detectors Based on a GaN High-Electron-Mobility Transistor with Integrated Bowtie Antennas. *Sensors* **2022**, *22*, 933. [[CrossRef](#)]
53. Jia, H.; Tang, X.; Zhu, X.; Li, M.; Wu, D.; Li, P.; Wang, J.; Li, M.; Li, J. Low-noise room-temperature terahertz detector based on the photothermoelectric effect of graphene oxide-Bi films. *Opt. Mater.* **2023**, *136*, 113432. [[CrossRef](#)]
54. Delgado-Notario, J.A.; Knap, W.; Clericò, V.; Salvador-Sánchez, J.; Calvo-Gallego, J.; Taniguchi, T.; Watanabe, K.; Otsuji, T.; Popov, V.V.; Fateev, D.V.; et al. Enhanced terahertz detection of multigate graphene nanostructures. *Nanophotonics* **2022**, *11*, 519–529. [[CrossRef](#)]
55. Guo, W.; Dong, Z.; Xu, Y.; Liu, C.; Wei, D.; Zhang, L.; Shi, X.; Guo, C.; Xu, H.; Chen, G.; et al. Sensitive Terahertz Detection and Imaging Driven by the Photothermoelectric Effect in Ultrashort-Channel Black Phosphorus Devices. *Adv. Sci.* **2020**, *7*, 1902699. [[CrossRef](#)] [[PubMed](#)]
56. Safin, A.; Puliafito, V.; Carpentieri, M.; Finocchio, G.; Nikitov, S.; Stremoukhov, P.; Kirilyuk, A.; Tyberkevych, V.; Slavin, A. Electrically tunable detector of THz-frequency signals based on an antiferromagnet. *Appl. Phys. Lett.* **2020**, *117*, 222411. [[CrossRef](#)]
57. Gayduchenko, I.; Xu, S.G.; Alymov, G.; Moskotin, M.; Tretyakov, I.; Taniguchi, T.; Watanabe, K.; Goltsman, G.; Geim, A.K.; Fedorov, G.; et al. Tunnel field-effect transistors for sensitive terahertz detection. *Nat. Commun.* **2021**, *12*, 543. [[CrossRef](#)]
58. Čibiraitė-Lukenskiėnė, D.; Ikamas, K.; Lissauskas, T.; Krozer, V.; Roskos, H.G.; Lissauskas, A. Passive Detection and Imaging of Human Body Radiation Using an Uncooled Field-Effect Transistor-Based THz Detector. *Sensors* **2020**, *20*, 4087. [[CrossRef](#)]

Disclaimer/Publisher's Note: The statements, opinions and data contained in all publications are solely those of the individual author(s) and contributor(s) and not of MDPI and/or the editor(s). MDPI and/or the editor(s) disclaim responsibility for any injury to people or property resulting from any ideas, methods, instructions or products referred to in the content.